IEEE Access
Multidisciplinary | Rapid Review | Open Access Journal

IEEE MAGNETICS SOCIETY SECTION

Received 2 March 2023, accepted 28 March 2023, date of publication 31 March 2023, date of current version 5 April 2023.

Digital Object Identifier 10.1109/ACCESS.2023.3263494

RESEARCH ARTICLE

Analytical Modeling of Rotary Electromagnetic Fault Current Limiter

SEYED AMIN FAZLJOO[1], ALIAKBAR DAMAKI ALIABAD[1], AND EBRAHIM AMIRI[2], (Senior Member, IEEE)

[1]Department of Electrical Engineering, Yazd University, Yazd 8915818411, Iran
[2]Department of Electrical and Computer Engineering, The University of New Orleans, New Orleans, LA 70148, USA

Corresponding author: Aliakbar Damaki Aliabad (alidamaki@yazd.ac.ir)

ABSTRACT Rotary electromagnetic fault current limiter (FCL) is an emerging technology for limiting fault currents in the power network. The device consists of two movable air-core spherical reactor rings (i.e., inner and outer rings). The movable feature allows the reactor rings to rotate, and form a proper mutual positional displacement. This can limit the fault current since the effective inductance of the device is dependent to the mutual angular position of the reactor rings. Due to the unconventional structure, to this date, the design process has solely been based on finite element (FE) method. This paper aims to analytically validate the theory and the overall functionality of the device in both the steady state and transient regime. For this propose, the resistance and the inductance of the device are first computed at normal operating condition using the basic theory of engineering electromagnetics. Next, performance characteristics such as electromagnetic torque, rotational displacement of the reactors, effective inductance of the device, and the network current are calculated at the faulty condition. For verification purposes, analytical results are compared with via FE simulation and experimental test.

INDEX TERMS Analytical model, electromagnetic fault current limiter, rotational motion, variable inductance.

I. INTRODUCTION

Fault current limiters (FCLs) are one of the most commonly used protection devices in the power network. The FCLs can be classified in different types such as Superconducting Fault current limiters (SFCLs) [1], [2], [3], [4], [5], [6], [7], [8], Solid-state Fault Current Limiters (SSFCLs) [9], [10], [11], [12], [13], Hybrid Fault Current Limiters FCLs (HFCLs) [14], [15], [16], Electromagnetic Fault Current Limiters (EMFCLs) [17], [18] and other technologies such as saturated type, liquid-metal type, PTC resistor type [19], [20], [21], [22].

To reduce the manufacturing and the operational costs associated with conventional electromagnetic FCLs, a rotary air-core electromagnetic FCL is introduced by authors in [23]. The presented device is characterized by small size, light-weight, simple structure, (since it does not require detection circuit, control system, and ferromagnetic core), low maintenance cost, acceptable response time, and reversible operation. However, the design process and the performance analysis of the presented device is only carried out numerically via Finite Element (FE) method. Despite the precision of the FE modeling, design procedure solely based on FE could get computationally costly, particularly during the optimization phase. In addition, it is often difficult to gain a physical insight and create a meaningful connection between design parameters, the performance of the device and its effect on the network solely based on the FE. Analytical and/or semi-analytical modeling techniques are relatively faster and also could serve as a reliable tool for design validation purposes. In the literature, various analytical techniques such as mesh or filament method [24] are available for calculating the self and the mutual inductance of coaxial and non-coaxial coils with arbitrary mutual position. In filament method, the cross sectional area of the coil is divided into multiple subsections, with each subsection being

The associate editor coordinating the review of this manuscript and approving it for publication was Philip Pong.

considered as a current filament in its center. In other words, the coil's cross section includes a set of current filaments. The self-inductance, mutual inductance and the magnetic force and torque between two current filaments can be formulated in terms of elliptical integrals of the first, second and third kind, Heuman's Lambda function, Bessel functions, and Legendre functions, and computed based on fundamental principle of engineering electromagnetics such as Maxwell equations, Neumann integral and Bio-savart law [25], [26]. Next, these relations are extended and applied to the entire cross section of the coil in order to compute the inductance and the torque between two coils [24], [25], [27], [28], [29], [30], [31], [32], [33], [34], [35], [36], [37]. In particular, in [33] the magnetic force between circular coils with non-parallel axes and rectangular cross section are computed by adding magnetic forces between all individual filaments. Using Grover's formula [38] and filament method Babic and Akyel obtained the torque between two filamentary circular coils with inclined axes [35]. However, existing models have mostly been applied/reported to co-axial and/or leveled, stationary coils with simple/standard geometrical shape (e.g., solenoid coil, disk-shape coil). To make the model compatible with the presented FCL device, proper adjustments must be made based on the geometrical shape of the two coils (i.e., spherical ring-shape coils). In addition, the inductance value and the electromagnetic between the coils should be continuedly updated in accordance with the angular displacement of the two coils.

Motivated by the merits of analytical modeling, and based on the fundamental concept of engineering electromagnetics this paper presents an analytical framework to validate the operational theory and to facilitate the design process of the newly developed rotary electromagnetic FCL. To fully capture the performance of the device, analytical modeling shall describe the main design parameters (e.g., resistance and inductance of coils), and the respective performance characteristic (e. g., torque between the coils, and the angular displacement of the coils, and etc). For this purpose, detailed performance characteristics of the device are computed at a faulty scenario, and compared against FE results. The presented model can be generalized and applied to coils with different structures and with arbitrary positions. This paper is organized as follows. Section II briefly describes the structure and the operating principle of the rotary electromagnetic FCL. Section III presents the analytical framework, followed up by related results and discussion in section IV. Finally, section V presents experimental validation.

II. STRUCTURE AND THE OPERATING PRINCIPLE

The structure of the presented air-core FCL includes two concentric spherical reactor rings as shown in Fig. 1. Both reactors are movable along polar angle (θ) in spherical coordinate system (Fig. 1), but to simplify explaining the concept, the outer reactor is assumed fixed/stationary here. The two reactor rings are connected in series (with reverse excitation current flow) from one end, and to the input/output terminal

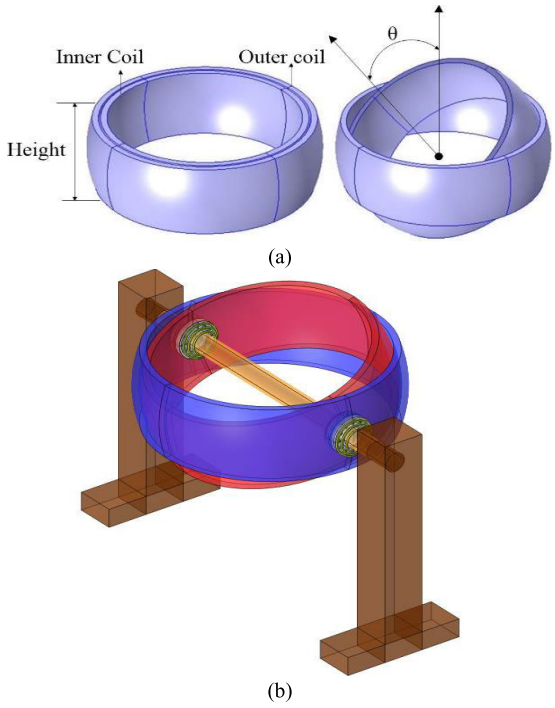

FIGURE 1. The structure of the rotary air core electromagnetic FCL, (a) reactor rings, (b) the entire structure [23].

of the device from the other end. The portable feature of the inner reactor ring allows the mutual angular displacement between the two reactors. Since the effective inductance of the device changes in correlation with the mutual angular displacement between the reactor rings, the device behaves like a variable inductance. Initially, the electromagnetic torque between the two coils is negligible, and the reactor rings are kept almost aligned with the help of an external force (i.e., spring force). In other words, in normal condition, the reactor rings are aligned (with minimal angular displacement), and thus the reactors' mutual inductance is relatively high. Considering the reverse excitation current flow of the reactor rings, the mutual and self-inductances have an opposite polarity. Therefore, the overall inductance/impedance of the device is initially low. Once the fault occurs in the network, it exerts a significant repulsive torque to the moving reactor, which results in a steady increase of the positional/angular displacement between the reactor rings as illustrated in Fig. 1. During this transition, the negative mutual inductance keeps declining until the inner and outer reactor rings are displaced by 90 degrees. At this stage, the negative mutual inductance becomes zero. Beyond this point (when the angular displacement reaches slightly above 90 degrees), the current flow of the inner reactor reverses and flow in a same direction as the current in the outer reactor. This converts the initial repulsive torque between the reactors to an attraction torque, and thus, the mutual displacement between the two reactor rings keeps rising up to 180 degrees. It is noted that during this transition (i.e., from 90 degrees to 180 degrees angular displacement) the polarity of the mutual inductance also reverses, and

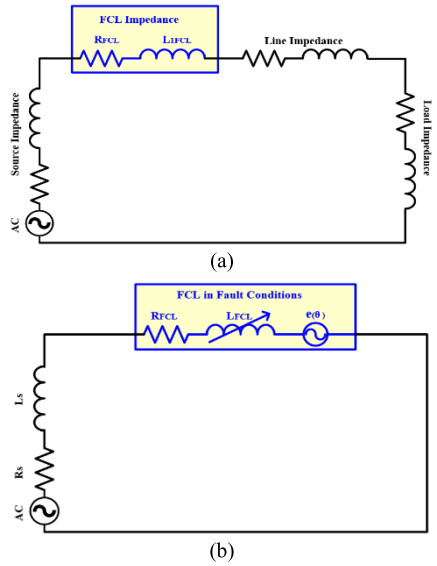

FIGURE 2. Circuit diagram of the power network with the FCL at (a) normal condition, (b) faulty condition.

becomes positive and similar to the self-inductance. Therefore, the total inductance of the device keeps rising up from 0 degrees to 180 degrees displacement, with the maximum inductance occurring at 180 degrees displacement. Once the fault is cleared and the electromagnetic attraction or repulsive torque is removed, and the external/spring force returns the movable reactor back to its initial/aligned position. To ensure that the device operates properly, initially the reactor rings must be slightly displaced to create sufficient amount of repulsive electromagnetic torque. If the angular displacement between the reactor rings is initially zero, the torques may cancel out and the equipment may not react to the short circuit current. The structure and the operating principle of the device is extensively explained in [23].

III. ANALYTICAL MODELING

A. EQUIVALENT CIRCUIT OF THE POWER NETWORK AT NORMAL AND FAULTY CONDITIONS

Fig. 2(a) illustrates the single circuit diagram of the power network with the FCL being connected to the network. At normal conditions, the circuit includes source impedance, FCL impedance, line impedance and the load impedance. As discussed in section II, the reactor rings are almost aligned and device exhibits a minimal inductance (L_{1FCL}).

At the transient stage of the faulty condition, the angular displacement between the reactors is continuously rising up from the initial angle (e.g., 15 degrees) to 180 degrees, which results in rapid and steady increase of the inductance. Therefore, the inductance of the device is represented by a variable inductance in the circuit diagram of Fig. 2(b). During the transient fault period, the rotary motion of the inner reactor induces a moving/rotational voltage, which is represented by $e(\theta)$ in the circuit diagram. After the transient period has passed and the two reactors are displaced by 180 degrees, the inductance of the device will be maximum.

The circuit model of the distribution network during this transient period can be described by the following set of relations [39]:

$$V_s = R_s i + L_s \frac{di}{dt} + R_{FCL} i + \frac{d\lambda(\theta.i)}{dt} \tag{1}$$

$$\lambda = L_{FCL}(\theta).i(t) \tag{2}$$

$$\frac{d\lambda(\theta.i)}{dt} = L_{FCL}(\theta)\frac{di}{dt} + \frac{d\theta}{dt}\frac{dL_{FCL}(\theta)}{d\theta} i = L_{FCL}(\theta)\frac{di}{dt} + \Omega\frac{dL_{FCL}(\theta)}{d\theta} i \tag{3}$$

$$e(\theta.i) = \Omega\frac{dL_{FCL}(\theta)}{d\theta} i \tag{4}$$

where, V_S, L_S, R_S, λ, L_{FCL}, R_{FCL}, θ, Ω and e are the source/network voltage, source inductance, source resistance, FCL flux linkage, FCL inductance, FCL resistance, angular position of the rotating (inner) coil with respect to the stationary (outer) coil, angular velocity of the rotating coil, and the induced rotational voltage (dependent voltage source) respectively.

The circuit model implies that the short circuit current is suppressed not only with the rise of the FCL inductance (L_{FCL}), but with the moving/rotational voltage (e) induced by the rotary motion of the inner reactor ring. The induced voltage is proportional to the angular velocity of the inner coil as expressed in (4). Inserting (2) into (1) yields:

$$\begin{aligned} &|V_m|\sin(\omega t+\delta) \\ &= R_s i + L_s\frac{di}{dt} + R_{FCL} i \\ &\quad + L_{FCL}(\theta)\frac{di}{dt} + \Omega\frac{dL_{FCL}(\theta)}{d\theta} i \\ &= \left(R_s + R_{FCL} + \Omega\frac{dL_{FCL}(\theta)}{d\theta}\right).i + (L_s + L_{FCL}(\theta))\frac{di}{dt} \\ &= \left(R_s + R_{FCL} + \Omega\frac{dL_{FCL}(\theta)}{d\theta}\right).i + (L_s + L_{FCL}(\theta))\frac{di}{dt} \end{aligned} \tag{5}$$

The short circuit current is given by:

$$I_{sc} = \frac{|V_m|}{|Z_{tn}|}\left[\sin(\omega t+\delta-\varphi) - e^{-\frac{R_s+R_{FCL}+\Omega\frac{dL_{FCL}(\theta)}{d\theta}}{L_s+L_{FCL}(\theta)}t}\sin(\delta-\varphi)\right] \tag{6}$$

$$|Z_{tn}| = \sqrt{\left(R_s+R_{FCL}+v\left(\theta\Omega\frac{dL_{FCL}(\theta)}{d\theta}\right)\right)^2+\omega^2(L_s+L_{FCL}(\theta))^2} \tag{7}$$

$$\varphi = \tan^{-1}\frac{\omega(L_s + L_{FCL}(\theta))}{\left(R_s + R_{FCL} + \Omega\frac{dL_{FCL}(\theta)}{d\theta}\right)} \tag{8}$$

where, V_m, Z_{tn}, δ, φ and ω are the peak value of the network phase voltage, equivalent network impedance at short circuit conditions, phase angle of the network voltage, phase angle of the network impedance, and the network

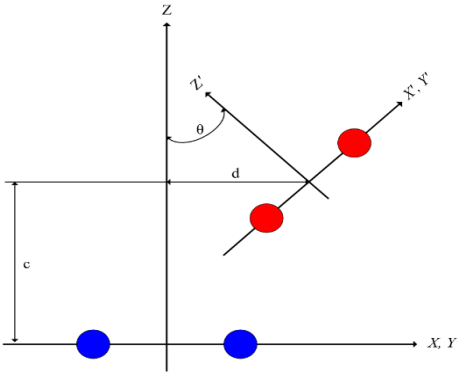

FIGURE 3. Two circular filaments with arbitrary positions [27].

frequency respectively. To accurately capture the response of the network to the fault, it is necessary to consider the behavior of the FCL device from the electrical, magnetic, and mechanical perspectives. For this purpose, electrical parameters (i.e., resistance, and inductance), the current and the torque are calculated within one operational cycle of the inner coil (i.e., from 15 degrees to 180 degrees angular displacement).

B. ELECTRICAL PARAMETERS OF THE FCL (RESISTANCE, SELF AND MURUAL INDUCTANCE)

The overall resistance of a coil is simply obtained by collecting the conductor's resistance at each turn as expressed in (4).

$$R_{coil} = \sum_{i=1}^{i=N} R_i \tag{9}$$

$$R_i = \rho \frac{l_i}{A} \tag{10}$$

$$l_i = 2\pi r_i \tag{11}$$

where $R_{coil}, R_i, N, \rho, l_i, A$, and r_i represent resistance of coil, resistance of each turn, turn number of each coil, special resistance of conductor, length of turn, cross section of conductor, and the radius of each turn, respectively.

In electromagnetics, the mutual inductance between two circular current filaments with arbitrary positions with respect to each other (Fig. 3) can be calculated by (12) and [27].

$$M = \frac{\mu_o \sqrt{R_p R_s}}{\pi} \times \int_0^{\pi} \frac{\left[\cos\theta - \frac{d}{R_s}\cos\varphi\right]\Psi(k)}{\sqrt{V^3}} d\varphi \tag{12-a}$$

where

$$V = \sqrt{1 - \cos\varphi^2 \sin\theta^2 - 2\frac{d}{R_s}\cos\varphi\cos\theta + \frac{d^2}{R_s^2}} \tag{12-b}$$

$$k^2 = \frac{4\alpha V}{(1+\alpha V)^2 + \zeta^2} \tag{12-c}$$

$$\zeta = \beta - \alpha\cos\varphi\sin\theta \tag{12-d}$$

$$\alpha = \frac{R_s}{R_p}.\beta = \frac{c}{R_p} \tag{12-e}$$

$$\Psi(k) = \left(\frac{2}{k} - k\right)K(k) - \frac{2}{k}E(k) = Q1/2(x) \tag{12-f}$$

$$K(k) = \int_0^{\frac{\pi}{2}} \frac{d\varphi}{\sqrt{1 - k^2 sin^2\varphi}} d\varphi \tag{12-g}$$

$$E(k) = \int_0^{\frac{\pi}{2}} \sqrt{1 - k^2 sin^2\varphi} d\varphi \tag{12-h}$$

where R_p, R_s, and θ are radius of primary filament, radius of secondary filament, and angle between z and z' axis, respectively. These parameters are visually illustrated in Fig. 3. The horizontal distance and vertical distance between two centers of filaments are shown by parameters c and d respectively. $K(k), E(k)$, and $Q1/2(x)$ are complete elliptic integral of the first kind, complete elliptic integral of the second kind and Legendre function of the second kind and half-integral degree respectively. μ_o is magnetic permeability of vacuum.

Based on the filament method, the cross sectional areas of two neighboring coils are modeled and considered by a set of current filaments as shown (with small white pixels) in Fig. 4. The mutual inductance between every two individual current filaments in coil# 1 and coil# 2 is obtained via (12), and the mutual inductance between the whole set of current filaments in coil# 1 and coil # 2 is obtained via Babic's relation (13) [27]. It is noted that Babic relation (13) is only valid for coils with rectangular shape cross section. However, in case of the presented FCL structure, the cross section of the reactor coils is spherical-shape (Fig. 5). Thus, the Babic's expression is modified and updated to be compatible with the spherical structure of the coils in the presented device. Applying proper adjustments on (13), the mutual inductance between two spherical coil rings with arbitrary positions with respect to each other takes the form (14):

$$M = \frac{N_1 N_2 \sum_{g=-K}^{g=K} \sum_{h=-N}^{h=N} \sum_{l=-N}^{l=N} \sum_{p=-m}^{p=m} M(g.h.l.p)}{(2S+1)(2N+1)(2m+1)(2n+1)} \tag{13-a}$$

where

$$M(g.h.l.p) = \frac{\mu_o \sqrt{R_p(h) R_s(l)}}{\pi} \times \int_0^{\pi} \frac{\left[\cos\theta - \frac{y(p)}{R_s(l)}\cos\varphi\right]\Psi(k)}{\sqrt{V^3}} d\varphi \tag{13-b}$$

$$V = \sqrt{1 - \cos\varphi^2 \sin\theta^2 - 2\frac{y(p)}{R_s(l)}\cos\varphi\cos\theta + \frac{y^2(p)}{R_s^2}} \tag{13-c}$$

$$k^2 = \frac{4\alpha V}{(1+\alpha V)^2 + \zeta^2} \tag{13-d}$$

$$\zeta = \beta - \alpha\cos\varphi\sin\theta \tag{13-e}$$

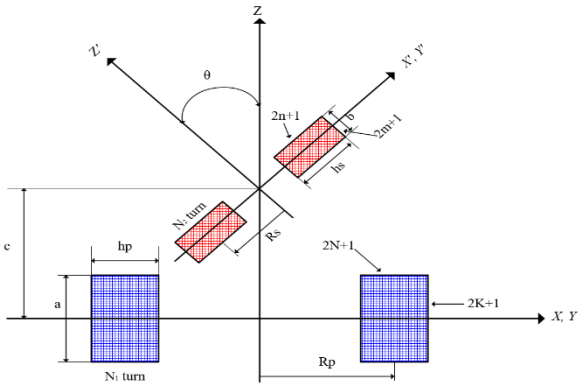

FIGURE 4. Two coils with rectangular cross section with angle θ with respect to each other [27].

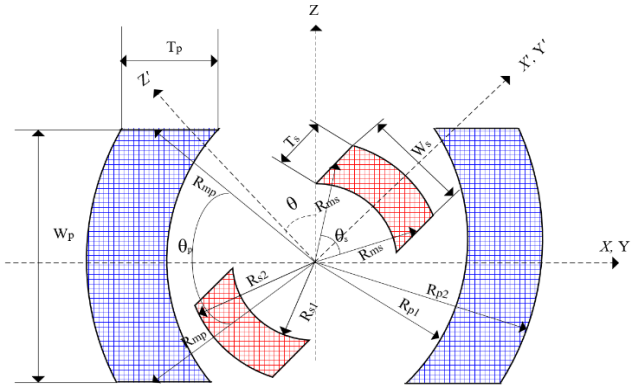

FIGURE 5. The cross-section of two spherical coil rings with arbitrary position with respect to each other.

$$\alpha = \frac{R_s}{R_p(h)}.\beta = \frac{z(g.p)}{R_p(h)} \tag{13-f}$$

$$\Psi(k) = \left(\frac{2}{k} - k\right) K(k) - \frac{2}{k} E(k) \tag{13-g}$$

$$y_o(p) = \frac{b\sin\theta}{(2m+1)} p \tag{13-h}$$

$$y(p) = d + y_o(p) = d + \frac{b\sin\theta}{(2m+1)} p \tag{13-i}$$

$$R_p(h) = R_p + \frac{h_p}{(2N+1)} h \tag{13-j}$$

$$R_p = \frac{R_1 + R_2}{2}.h_p = R_2 - R_1 \tag{13-k}$$

$$R_s(l) = R_s + \frac{h_s}{(2N+1)} l \tag{13-l}$$

$$R_s = \frac{R_3 + R_4}{2}.h_s = R_4 - R_3 \tag{13-m}$$

$$z(g.p) = c + \frac{a}{(2K+1)} g - \frac{b\cos\theta}{(2m+1)} p \tag{13-n}$$

$$h = -N \ldots .0 \ldots .N$$
$$g = -K \ldots .0 \ldots .K$$
$$l = -n \ldots .0 \ldots .n$$
$$p = -m \ldots .0 \ldots .m \tag{13-o}$$

where (14-a), as shown at the bottom of the next page,

$$M\left(n_{wp}.n_{tp}.n_{ws}.n_{ts}\right) = \frac{\mu_o \sqrt{R_p(n_{wp}.n_{tp}) R_s(n_{ws}.n_{ts})}}{\pi} \times \int_0^{\pi} \frac{[\cos\theta - \gamma\cos\varphi]\,\Psi(k)}{\sqrt{V}^3} d\varphi \tag{14-b}$$

$$V = \sqrt{1 - \cos\varphi^2 \sin\theta^2 - 2\gamma\cos\varphi\cos\theta + \gamma^2} \tag{14-c}$$

$$k^2 = \frac{4\alpha V}{(1+\alpha V)^2 + \zeta^2} \tag{14-d}$$

$$\zeta = \beta - \alpha\cos\varphi\sin\theta \tag{14-e}$$

$$\alpha = \frac{R_s(n_{ws}.n_{ts})}{R_p(n_{wp}.n_{tp})}.\beta = \frac{z(n_{wp}.n_{ws})}{R_p(n_{wp}.n_{tp})} \tag{14-f}$$

$$\gamma = \frac{y(n_{ws})}{R_s(n_{ws}.n_{ts})} \tag{14-g}$$

$$R_p(n_{wp}.n_{tp}) = R_{mp}\cos\left(\frac{\theta_p}{2N_{wp}+1} n_{wp}\right) + \frac{T_p}{(2N_{tp}+1)} n_{tp} \tag{14-h}$$

$$R_s(n_{ws}.n_{ts}) = R_{ms}\cos\left(\frac{\theta_s}{2N_{ws}+1} n_{ws}\right) + \frac{T_s}{(2N_{ts}+1)} n_{ts} \tag{14-i}$$

$$y(n_{ws}) = R_{ms}\sin\left(\frac{\theta_s}{2N_{ws}+1} n_{ws}\right)\sin\theta \tag{14-j}$$

$$z(n_{wp}.n_{ws}) = R_{mp}\sin\left(\frac{\theta_p}{2N_{wp}+1} n_{wp}\right)\sin\theta - R_{ms}\sin\left(\frac{\theta_s}{2N_{ws}+1} n_{ws}\right)\cos\theta \tag{14-k}$$

$$R_{mp} = \frac{R_{p1} + R_{p2}}{2} \tag{14-l}$$

$$R_{ms} = \frac{R_{s1} + R_{s2}}{2} \tag{14-m}$$

$$\theta_p = 2\sin^{-1}\left(\frac{W_p}{2R_{mp}}\right) \tag{14-n}$$

$$\theta_s = 2\sin^{-1}\left(\frac{W_s}{2R_{ms}}\right) \tag{14-o}$$

$$T_p = R_{p2} - R_{p1}.T_s = R_{s2} - R_{s1} \tag{14-p}$$

$$\Psi(k) = \left(\frac{2}{k} - k\right) K(k) - \frac{2}{k} E(k) \tag{14-q}$$

$$n_{wp} = -N_{wp} \ldots .0 \ldots .N_{wp}$$
$$n_{tp} = -N_{tp} \ldots .0 \ldots .N_{tp}$$
$$n_{ws} = -N_{ws} \ldots .0 \ldots .N_{ws}$$
$$n_{ts} = -N_{ts} \ldots .0 \ldots .N_{ts} \tag{14-r}$$

The self-inductance is calculated by the filament method as a special case of the mutual inductance between two coils. In other words, the self-inductance of a coil can be regarded as the mutual inductance between two identical and coincided coils. The presented method is general and is valid irrespective of wiring arrangement and/or the size/dimension of the

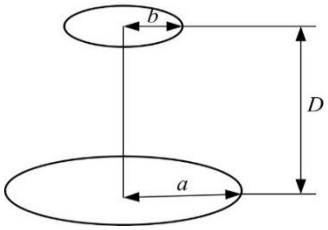

FIGURE 6. Two current filaments with a same axis.

coil. Therefore, the self-inductance is modeled and calculated as the mutual inductance between two filaments located along the same axis as shown in Fig. 6, when the angle between z and z' axis (θ), and the distance between the centers of filaments are both set to zero (15). In fact, relation (15) is a special case of relation (12) when parameters θ and c are set to zero.

$$M = \mu\sqrt{ab}\left[\left(\frac{2}{k} - k\right)K(k) - \frac{2}{k}E(k)\right] \tag{15-a}$$

$$k^2 = \frac{4ab}{D^2 + (a+b)^2} \tag{15-b}$$

where a, b, and D are radius of primary filament, radius of secondary filament, and distance between center of two filaments, respectively.

For this purpose, the cross-sectional area of the coil is divided into multiple segments and the mutual inductance value between every two filament segments is calculated using (15). Finally, the self-inductance of the coil is obtained by adding the mutual inductance of all filament segments as expressed in (16).

$$L = \frac{N^2}{n^2}\sum_{i=1}^{n}\sum_{j=1}^{n} Mij.i \neq j \tag{16}$$

where Mij is the mutual inductance between filament i and j which is calculated by (15). N and n are turn number of coil and number of segment (mesh) respectively.

C. ELECTOMAGNETIC TORQUE

The electromagnetic torque between the inner and outer reactor rings can be computed via meshing method (similar to inductance calculation) by segmenting the coil into multiple current carrying filaments. Suppose that current I_1 and I_2 pass through two filaments with the mutual inductance of M. The torque between the two filaments is obtained by the product of the two currents and the derivative of their mutual inductance as expressed in (17). Inserting proper form of mutual inductance in (17), the torque between two coils with rectangular cross section is obtained by (18), and for spherical cross section is obtained by (19).

$$\tau = -I_1 I_2 \frac{\partial M}{\partial \theta} \tag{17}$$

$$\tau = \frac{\mu_o}{\pi} I_1 I_2 \sqrt{R_p R_s} \times \int_0^{\pi} \frac{F_1(\varphi.\theta)\,\Psi(k) + F_2(\varphi.\theta)\Phi(k)}{\sqrt{V}^3} d\varphi \tag{18-a}$$

$$F_1(\varphi.\theta) = \sin\theta + \frac{3(-\cos^2\varphi \sin\theta\cos\theta + \frac{d}{R_s}\cos\varphi\sin\theta)}{2} \times \frac{\cos\theta - \frac{d}{R_s}\cos\varphi}{\sqrt{V}} \tag{18-b}$$

$$F_2(\varphi.\theta) = (\cos\theta - \frac{d}{R_s}\cos\varphi)\left(\frac{k'}{k^2}\right) \tag{18-c}$$

$$\Psi(k) = \left(\frac{2}{k} - k\right)K(k) - \frac{2}{k}E(k) \tag{18-d}$$

$$V = \sqrt{1 - \cos^2\varphi\sin\theta^2 - 2\frac{d}{R_s}\cos\varphi\cos\theta + \frac{d^2}{R_s^2}} \tag{18-e}$$

$$k^2 = \frac{4\alpha V}{(1+\alpha V)^2 + \zeta^2} \tag{18-f}$$

$$k' = \frac{\alpha\left[\frac{-\cos^2\varphi\sin\theta\cos\theta + \frac{d}{R_s}\cos\varphi\sin\theta}{V}\right]\left[\frac{2}{k} - k(1+\alpha V)\right] + \alpha k\zeta\cos\varphi}{(1+\alpha V)^2 + \zeta^2} \tag{18-g}$$

$$\zeta = \beta - \alpha\cos\varphi\sin\theta \tag{18-h}$$

$$\alpha = \frac{R_s}{R_p}.\beta = \frac{c}{R_p} \tag{18-i}$$

where (19-a), as shown at the bottom of the next page,

$$\tau = \frac{\mu_o}{\pi} I_1 I_2 \sqrt{R_s(n_{ws}.n_{ts})\,R_p(n_{wp}.n_{tp})} \times \int_0^{\pi} \frac{F_1(\varphi.\theta)\,\Psi(k) + F_2(\varphi.\theta)\Phi(k)}{\sqrt{V}^3} d\varphi \tag{19-b}$$

$$R_p(n_{wp}.n_{tp}) = R_{mp}\cos\left(\frac{\theta_p}{2N_{wp}+1}n_{wp}\right) + \frac{T_p}{(2N_{tp}+1)}n_{tp} \tag{19-c}$$

$$R_s(n_{ws}.n_{ts}) = R_{ms}\cos\left(\frac{\theta_s}{2N_{ws}+1}n_{ws}\right) + \frac{T_s}{(2N_{ts}+1)}n_{ts} \tag{19-d}$$

$$F_1(\varphi.\theta) = (\sin\theta + \gamma'\cos\varphi) + \frac{3W}{2} \times \frac{(\cos\theta - \gamma\cos\varphi)}{\sqrt{V}} \tag{19-e}$$

$$M = \frac{N_1 N_2 \sum_{n_{wp}=-N_{wp}}^{n_{wp}=N_{wp}} \sum_{n_{tp}=-N_{tp}}^{n_{tp}=N_{tp}} \sum_{n_{ws}=-N_{ws}}^{n_{ws}=N_{ws}} \sum_{nts=-N_{ts}}^{nts=N_{ts}} M\left(n_{wp}.n_{tp}.n_{ws}.n_{ts}\right)}{(2N_{wp}+1)(2N_{tp}+1)(2N_{ws}+1)(2N_{ts}+1)} \tag{14-a}$$

$$F_2(\varphi.\theta) = (\cos\theta - \gamma\cos\varphi)\left(\frac{k'}{k^2}\right) \tag{19-f}$$

$$V = \sqrt{1-\cos^2\varphi\sin\theta^2 - 2\gamma\cos\varphi\cos\theta+\gamma^2} \tag{19-g}$$

$$k^2 = \frac{4\alpha V}{(1+\alpha V)^2+\zeta^2} \tag{19-h}$$

$$k' = \frac{\alpha V'\left[\frac{2}{k} - k(1+\alpha V)\right] - k\zeta\zeta'}{(1+\alpha V)^2+\zeta^2} \tag{19-i}$$

$$W = -\cos^2\varphi\sin\theta\cos\theta + \gamma\cos\varphi\sin\theta - \gamma'\cos\varphi\cos\theta + \gamma\gamma' \tag{19-j}$$

$$V' = \frac{W}{V} \tag{19-k}$$

$$\alpha = \frac{R_s(n_{ws}.n_{ts})}{R_p(n_{wp}.n_{tp})}.\beta = \frac{z(n_{wp}.n_{ws})}{R_p(n_{wp}.n_{tp})} \tag{19-l}$$

$$\gamma = \frac{y(n_{ws})}{R_s(n_{ws}.n_{ts})}.\zeta = \beta - \alpha\cos\varphi\sin\theta \tag{19-m}$$

$$y(n_{ws}) = R_{ms}\sin\left(\frac{\theta_s}{2N_{ws}+1}n_{ws}\right)\sin\theta \tag{19-n}$$

$$z(n_{wp}.n_{ws}) = R_{mp}\sin\left(\frac{\theta_p}{2N_{wp}+1}n_{wp}\right)\sin\theta - R_{ms}\sin\left(\frac{\theta_s}{2N_{ws}+1}n_{ws}\right)\cos\theta \tag{19-o}$$

$$R_{mp} = \frac{R_{p1}+R_{p2}}{2} \tag{19-p}$$

$$R_{ms} = \frac{R_{s1}+R_{s2}}{2} \tag{19-q}$$

$$\theta_p = 2\sin^{-1}\left(\frac{W_p}{2R_{mp}}\right) \tag{19-r}$$

$$\theta_s = 2\sin^{-1}\left(\frac{W_s}{2R_{ms}}\right) \tag{19-s}$$

$$T_p = R_{p2} - R_{p1}.T_s = R_{s2} - R_{s1} \tag{19-t}$$

$$\zeta' = \beta' - \alpha\cos\varphi\cos\theta \tag{19-u}$$

$$\gamma' = \frac{R_{ms}}{R_s(n_{ws}.n_{ts})}\sin\left(\frac{\theta_s}{2N_{ws}+1}n_{ws}\right)\cos\theta \tag{19-v}$$

$$\beta' = \frac{R_{mp}}{R_p(n_{wp}.n_{tp})}\sin\left(\frac{\theta_s}{2N_{ws}+1}n_{ws}\right)\sin\theta \tag{19-w}$$

$$n_{wp} = -N_{wp}.....0.....N_{wp}$$
$$n_{tp} = -N_{tp}.....0.....N_{tp}$$
$$n_{ws} = -N_{ws}.....0.....N_{ws}$$
$$n_{ts} = -N_{ts}.....0.....N_{ts} \tag{19-x}$$

D. MECHANICAL PARAMETERS OF THE FCL

The electromagnetic torque caused by the fault current moves the inner reactor (from the initial aligned position to 180 degrees angular displacement with respect to the stationary reactor). As a result, the overall inductance of the device rises up to a level that can effectively suppress the short circuit current. The mechanical operation of the moving reactor can be realized via the following formulations:

$$T_{mag} - T_{spring} = I\alpha \tag{20}$$

$$T_{spring} = k\Delta\theta \tag{21}$$

$$\Omega = \alpha t + \Omega_o \tag{22}$$

$$\theta_1 = \frac{1}{2}\alpha_1 t^2 + \Omega_1 t + \theta_{1o} \tag{23}$$

$$\theta_2 = \frac{1}{2}\alpha_2 t^2 + \Omega_2 t + \theta_{2o} \tag{24}$$

$$\theta = \theta_1 + \theta_2 \tag{25}$$

where, T_{mag}, T_{spring}, I, α, k, Ω_o, and θ_o are electromagnetic torque, spring torque, the moment of inertia of the inner coil, angular acceleration, spring constant, initial angular speed, and the initial angle with respect to Z axis, respectively.

Since the mass and the radius of the two reactor rings are different, the polar angle θ is calculated separately for each of the two coils as expressed in (23) and (24). Therefore, the overall angle between the reactors is equal to the sum of the angle of the moving reactors (25).

TABLE 1. Data of proposed EMFCL.

Inner Coil Outer Diameter	Value 1120	Unit mm	Outer Coil Outer Diameter	Value 1200	Unit Mm
Inner Diameter	1060	mm	Inner Diameter	1140	Mm
Height	400	mm	Height	400	Mm
Turn number	24		Turn Number	24	
Mass	170	kg	Mass	180	Kg

TABLE 2. Data of simulated power network.

Parameter	Value	Unit
Source Voltage (Phase-to-Phase)	20	kV
Power Frequency	50	Hz
Source Inductance	2.5	mH
Source Resistance	0.03	Ω
Max Load Power	12.5	MVA

IV. RESULT AND DISCUSSION

For verification purposes, analytical results are compared with those obtained from 3-D FE software package. Specifications of the presented case study (i.e., FCL and the distribution network) are adopted based on existing FCLs in practical/realistic power networks as listed in Table 1 and Table 2, respectively.

The initial angle θ between the z axis of the two reactor rings is initially set to 15° before the fault. This angle rises up to 180° within 20 ms (i.e., equivalent to one fault cycle). At this stage of operation (when the two reactor rings are

$$M = \frac{N_1N_2\sum_{n_{wp}=-N_{wp}}^{n_{wp}=N_{wp}}\sum_{n_{tp}=-N_{tp}}^{n_{tp}=N_{tp}}\sum_{n_{ws}=-N_{ws}}^{n_{ws}=N_{ws}}\sum_{nts=-N_{ts}}^{nts=N_{ts}} M\left(n_{wp}.n_{tp}.n_{ws}.n_{ts}\right)}{(2N_{wp}+1)(2N_{tp}+1)(2N_{ws}+1)(2N_{ts}+1)} \tag{19-a}$$

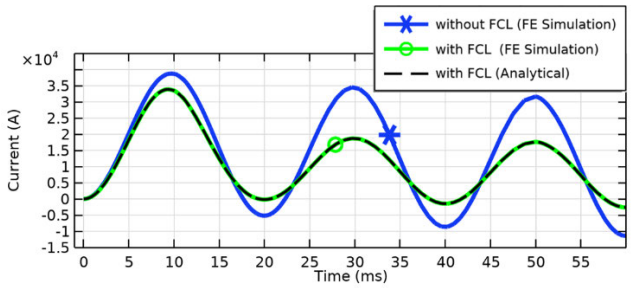

FIGURE 7. Short circuit current waveform.

TABLE 3. Cacluation and FE simulaed fault current.

Time (ms)	Current (kA)		Error Percentage
	Analytical	FE	%
0	0	0	0.00
1	0.915	0.915	-0.0085
2	3.557	3.556	0.2556
3	7.642	7.641	0.6641
4	12.748	12.744	1.1744
5	18.337	18.334	1.7334
6	23.815	23.810	2.2810
7	28.555	28.550	2.7550
8	31.959	31.954	3.0954
9	33.524	33.518	3.2518
10	32.947	32.939	3.1939
11	30.314	30.303	2.9303
12	26.217	26.208	2.5208
13	21.420	21.414	2.0414
14	16.403	16.399	1.5399
15	11.535	11.533	1.0533
16	7.153	7.152	0.6152
17	3.545	3.544	0.2544
18	0.927	0.925	-0.0077
19	-0.590	-0.592	-0.1589
20	-1.034	-1.037	-0.2034

displaced by 180°), the overall inductance of the FCL device does reach to its peak value. Although, it takes 20 ms for the two reactors to arrive at the final/optimal position for maximum inductance, the FCL device starts limiting the short circuit current from the very beginning as soon as the fault occurs. Fig. 7 presents the calculated and simulated short circuit current waveform within three fault cycles (i.e., 0 to 60 ms). For a more detailed observation, the amplitude of the fault current is presented at different time instants in Table 3. As observed, the discrepancy between the calculated and the FE simulated fault current values is very negligible, and is less than 3% in most instances. This validates the accuracy of the presented analytical model.

In addition, Fig. 7 illustrates that the presented FCL can successfully reduce the fault current in the network by approximately up to 45%. This confirms the functionality of the presented FCL.

To further evaluate the accuracy of the presented model, the self-inductance, mutual inductance and total inductance of the presented FCL are calculated within the first fault cycle (i.e., 0 to 20 ms), and compared against the FE simulation results (Figs 8 and 9). For a more detailed observation, the calculated and simulated inductance values and their respective percentage error are presented in Tables 4, 5 and 6.

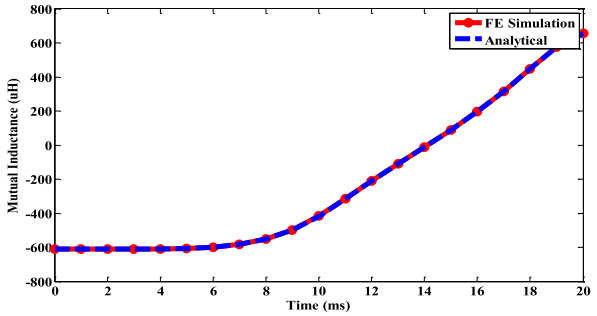

FIGURE 8. The rate of change of the mutual inductance.

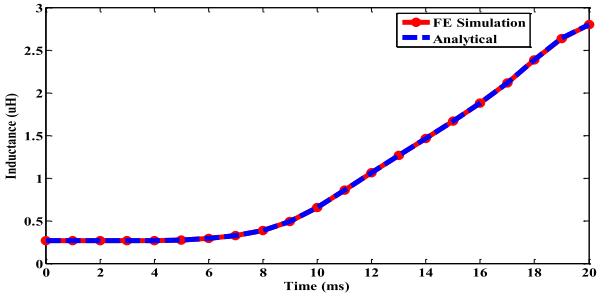

FIGURE 9. The rate of change of the total inductance.

TABLE 4. Cacluation and FE simulaed self inductance.

Coil	Self-Inductance (mH)		Error Percentage
	Analytical	FE	%
Inner	0.70238	0.70233	-0.0071
Outer	0.78567	0.78567	0.00

TABLE 5. Cacluation and FE simulaed mutual inductance.

Time (ms)	Mutual Inductance (uH)		Error Percentage
	Analytical	FEM	%
0	610.711	610.369	-0.0560
1	610.711	610.369	-0.0560
2	610.711	610.368	-0.0562
3	610.711	610.179	-0.0872
4	609.537	609.200	-0.0553
5	606.429	606.093	-0.0554
6	598.843	598.515	-0.0548
7	582.789	582.468	-0.0551
8	552.271	551.879	-0.0710
9	499.037	498.578	-0.0921
10	417.615	416.900	-0.1715
11	315.879	315.169	-0.2253
12	211.977	211.379	-0.2829
13	110.898	110.465	-0.3920
14	11.3384	11.119	-1.9732
15	89.6000	89.501	-0.1106
16	196.025	195.691	-0.1707
17	314.033	313.371	-0.2113
18	448.316	447.223	-0.2444
19	575.761	574.591	-0.2036
20	656.698	655.939	-0.1157

TABLE 6. Cacluation and FE simulaed total inductance.

Time (ms)	Inductance (mH)		Error Percentage %
	Analytical	FE	
0	0.26663	0.26715	0.1946
1	0.26663	0.26715	0.1946
2	0.26663	0.26715	0.1946
3	0.26663	0.26753	0.3364
4	0.26898	0.26949	0.1892
5	0.27519	0.27570	0.1850
6	0.29036	0.29086	0.1719
7	0.32247	0.32295	0.1486
8	0.38351	0.38413	0.1614
9	0.48998	0.49073	0.1528
10	0.65282	0.65409	0.1942
11	0.85629	0.85755	0.1469
12	1.06410	1.06513	0.0967
13	1.26625	1.26696	0.0560
14	1.46537	1.46565	0.0191
15	1.66725	1.6669	-0.0210
16	1.88010	1.8792	-0.0479
17	2.11612	2.11463	-0.0705
18	2.38468	2.382335	-0.0984
19	2.63957	2.637071	-0.0948
20	2.80145	2.7998	-0.0589

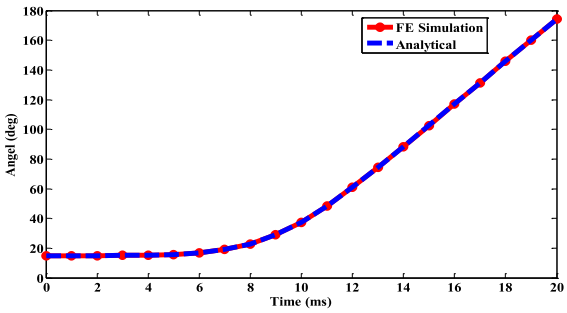

FIGURE 10. The angular displacement between the two coils during once fault cycle.

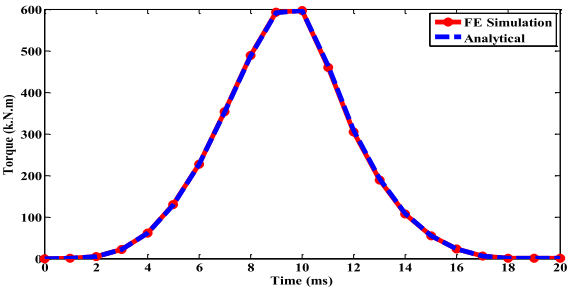

FIGURE 11. The profile of the electromagnetic torque between the two coils during one fault cycle.

TABLE 7. Cacluation and FE simulaed angelular displacmenet.

Time (ms)	Angel (deg)		Error Percentage %
	Analytical	FEM	
0	15.00	15.00	0
1	15.00	15.00	0
2	15.00	15.00	0
3	15.03	15.03	0
4	15.18	15.18	0
5	15.65	15.65	0
6	16.76	16.76	0
7	18.97	18.97	0
8	22.81	22.82	0.0438
9	28.86	28.88	0.0693
10	37.45	37.50	0.1333
11	48.42	48.48	0.1238
12	60.96	61.02	0.0983
13	74.41	74.46	0.0672
14	88.39	88.42	0.0339
15	102.64	102.63	-0.0097
16	116.99	116.962	-0.0239
17	131.37	131.315	-0.0419
18	145.75	145.662	-0.0604
19	160.11	160.00	-0.0688
20	174.47	174.335	-0.0774

TABLE 8. Cacluation and FE simulaed electromagnetic torque.

Time (ms)	Torque (kN.m)		Error Percentage %
	Analytical	FEM	
0	0	0	0
1	0.311	0.313	0.6390
2	4.708	4.720	0.2542
3	21.760	21.356	-1.8917
4	60.956	61.148	0.3140
5	128.703	129.244	0.4186
6	226.938	227.423	0.2133
7	351.952	352.768	0.2313
8	487.382	488.850	0.3003
9	591.881	593.033	0.1943
10	596.989	597.23	0.0404
11	463.447	460.296	-0.6846
12	308.777	305.069	-1.2155
13	190.822	188.621	-1.1669
14	108.590	107.136	-1.3572
15	54.762	54.085	-1.2517
16	22.644	22.399	-1.0938
17	6.324	6.284	-0.6365
18	0.471	0.470	-0.2128
19	0.154	0.156	1.2821
20	0.186	0.186	0

Fig. 10 presents the profile of the calculated and simulated angular displacement of the moving coils within the first fault cycle (i.e., 0 to 20 ms). It is seen that the two coils transit from the initial angle of 15° to the final angle of 180° within 20 seconds after the fault. Fig. 11 presents the calculated and simulated electromagnetic torque between the two coils within the same time period. The torque is initially small due to a relatively low current amplitude in the first few milliseconds. However, the torque rises rapidly (proportional to the current amplitude) and separates the two coils away within a short time frame. For more detailed information, Tables 7 and 8 present the percentage error between the presented analytical model and FE simulation at different time instants.

Both the modeling and simulation are performed on a computer with the specifications of: Intel(R) Core(TM) i7-7700HQ CPU @ 2.80GHz, RAM 16.0 GB.

For the given computer workstation computing power, the processing time of the presented model per time step varies between 37 *s* to 50 *s* (depending upon the angle between the

TABLE 9. Data/specification of the prototyped EMFCL.

Inner Coil	Value	Unit	Outer Coil	Value	Unit
Inner Diameter	180	mm	Inner Diameter	212	mm
Outer Diameter	202	mm	Outer Diameter	234	mm
Height	50	mm	Height	50	mm
Turn number	160		Turn Number	160	

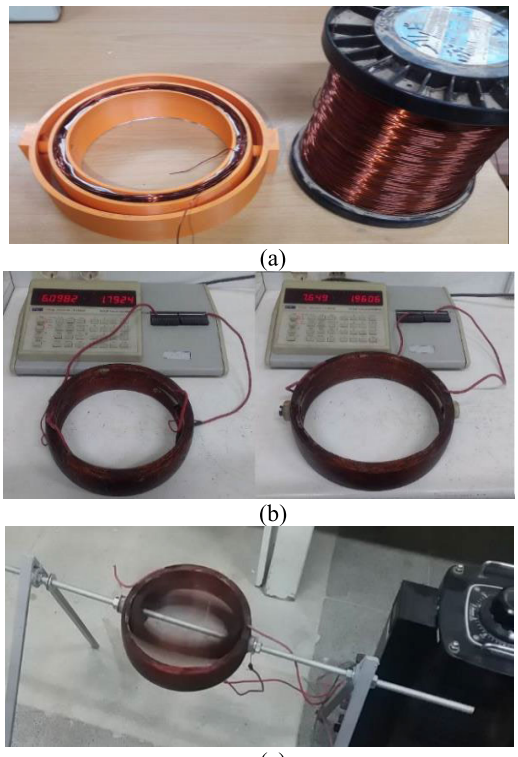

FIGURE 12. Laboratory testbed with down-scale prototype of the proposed FCL, (a) fabrication process, (b) self-inductance measurement, and (c) experimental test [23].

TABLE 10. Measured and simulated self-inductance.

Coil	Measured (mH)	Calculated (mH)	Error %
Inner	6.09	6.17	1.3
Outer	7.65	7.77	1.5

coils), whereas the processing time of the FEM model varies between 450 *s* to 520 *s*.

V. EXPREMENTAL RESULT

A down-scale prototype of the proposed FCL is built and tested to verify the functionality of the proposed device in the laboratory environment (Fig. 12). The coils are shaped in a plastic frame and mixed with an epoxy resin to produce void-free insulation between conductors and to improve the mechanical strength. Once the resin is dried and solid the coils are removed from the plastic frame. The data and specification of the prototyped model is presented in Table 9. The self and mutual inductance of the coils are measured and compared with the calculated values in Tables 10 and 11.

TABLE 11. Measured and simulated total inductance.

Displacement Angle (deg)	Measured (mH)	Calculated (mH)
0	3.54	3.42
10	3.87	3.92
20	4.97	5.14
30	6.46	6.66
40	7.90	8.14
50	9.16	9.46
60	10.34	10.68
70	11.48	11.80
80	12.52	12.88
90	13.72	13.94
100	14.48	15.00
110	15.90	16.08
120	16.98	17.20
130	18.11	18.42
140	19.45	19.74
150	20.95	21.22
160	22.53	22.74
170	23.88	23.96
180	24.40	24.46

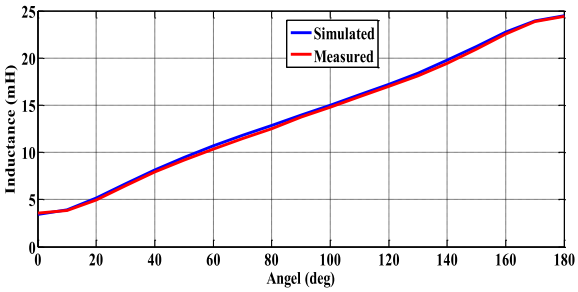

FIGURE 13. Measured and simulated total-inductance of the coils under test at different angular displacement.

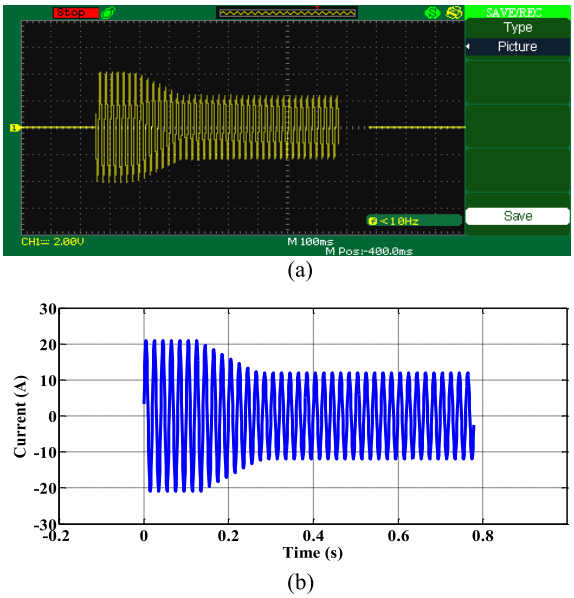

FIGURE 14. Emulating short circuit current by exciting the FCL with 100 V source voltage, (a) measured, and (b) calculated.

The profile of the total FCL inductance at different angular displacmenets between the coils is plotted in Fig. 13.

To emulate the fault current in the FCL, the prototyped model is supplied by a 50 Hz and 100 V (Phase-to-Neutral)

source voltage and the reaction of the inner coil is videoed and recorded. Consistent with the theory discussed in section II, the moving(inner) reactor reacted/rotated quickly and eventually came into rest at 180 degrees positional displacement with the outer reactor. In this test, the outer coil is kept stationary. The FCL current is measured by a digital oscilloscope and shown in Fig. 14 along with the calculated current waveform. As seen, calculated and measured current waveforms are in a good agreement. Since the supply voltage of the laboratory test is scaled down to 100V, the FCL response time is higher than the desireable time, but if the prototyped device was to get excited by higher voltage levels (e.g., 1000 V), the response time would be as low as 15 ms.

VI. CONCLUSION

The coreless electromagnetic FLC with rotational motion is an emerging technology for limiting fault currents in the power network. FE results reported in [23] showed a swift and effective response from the presented FCL to the fault in the network. In this paper, the theory and the functionality of the device was validated analytically using the fundamental concept of engineering electromagnetics. For this purpose, detailed electromagnetic parameters (i.e., resistance and inductance), the performance metrics of the device (i.e., torque between the coils, the angular displacement), and the amplitude of the fault current were computed and compared against FE simulation and measurement results. The calculated, simulated and measured results are in good agreement, indicating that the presented model features the operational excellency both in terms of computational speed, and also precision. In particular, for the given computer workstation computing power, the processing time of the presented model per time step was in the range of 37 *s* to 50 *s,* whereas the processing time of the FE model was in the range 450 *s* to 520 *s*.

It is noted that the simulation results presented in the paper and the 20 ms response time of the FCL are all captured when the FCL equipment was applied to a practical power grid with realistic power level, voltage level (i.e., 20 kV) and current level. Only the size of the prototyped model and the power and voltage levels of the experimental section are scaled down to laboratory levels. Although the FE simulation is carried out in medium voltage ranges (i.e., 20 kV), the use of composite material in between the coils (thickness of 10 mm) can provide insulation at higher voltage levels. It is also noted that the presented device in this article has a basic design. Research work to optimize the design and maximize the operating speed is ongoing and will be reported in a separate paper. The optimal design not only includes optimized size/dimensions but also incorporates light composite material and aluminum conductors (as opposed to copper conductors) to lower the weight and reduce the operating time.

REFERENCES

[1] B. V. Vaishnavi, R. S. A. Suji, D. P. Trivenishree, N. Nidha, and G. J. Sowmya, "Superconducting fault current limiter & its application," *Int. J. Sci. Eng. Res.*, vol. 7, no. 5, pp. 126–134, May 2016.

[2] V. V. Rao and S. Kar, "Superconducting fault current limiters—A review," *Indian J. Cryogenics*, vol. 36, pp. 14–25, Jan. 2011.

[3] M. Young and W. Hassenzahl, "Superconducting fault current limiters: Technology watch 2009," Electr. Power Res. Inst. (EPRI), Palo Alto, Santa Clara, CA, USA, Tech. Rep. 1017793, 2009.

[4] L. Ye and A. Campbell, "Behavior investigation of superconducting fault current limiters in power systems," *IEEE Trans. Appl. Supercond.*, vol. 16, no. 2, pp. 662–665, Jun. 2006.

[5] H. Kraemer, A. Bauer, M. Frank, P. van Hasselt, P. Kummeth, M. Wohlfart, C. Schacherer, T. Arndt, and T. Janetschek, "ASSiST—A superconducting fault current limiter in a public electric power grid," *IEEE Trans. Power Del.*, vol. 37, no. 1, pp. 612–618, Feb. 2022.

[6] W. Song, X. Pei, J. Xi, and X. Zeng, "A novel helical superconducting fault current limiter for electric propulsion aircraft," *IEEE Trans. Transport. Electrific.*, vol. 7, no. 1, pp. 276–286, Mar. 2021.

[7] Y. Guo, C. Huang, and J. Zhao, "Resonance type superconducting fault current limiters: Theory and applications," in *Proc. IEEE Int. Conf. Appl. Supercond. Electromagn. Devices (ASEMD)*, Oct. 2020, pp. 1–2.

[8] A. M. A. Ibrahim, I. Hamdan, S. F. Al-Gahtani, H. S. Hussein, L. S. Nasrat, and M. A. Ismeil, "Optimal shunt-resonance fault current limiter for transient stability enhancement of a grid-connected hybrid PV/wind power system," *IEEE Access*, vol. 9, pp. 126117–126134, 2021.

[9] C. A. Ordóñez, A. Gómez-Expósito, and J. M. Maza-Ortega, "Series compensation of transmission systems: A literature survey," *Energies*, vol. 14, no. 6, p. 1717, Mar. 2021.

[10] D. Philpott and L. Qi, "Solid-state fault current limiters for residential houses and commercial buildings," *IEEE Trans. Ind. Appl.*, vol. 55, no. 4, pp. 3431–3436, Jul. 2019.

[11] A. Abramovitz and K. M. Smedley, "Survey of solid-state fault current limiters," *IEEE Trans. Power Electron.*, vol. 27, no. 6, pp. 2770–2782, Jun. 2012.

[12] T. Ueda, M. Morita, H. Arita, Y. Kida, Y. Kurosawa, and T. Yamagiwa, "Solid-state current limiter for power distribution system," *IEEE Trans. Power Del.*, vol. 8, no. 4, pp. 1796–1801, Oct. 1993.

[13] R. Wang, Y. Chen, J. Chen, L. Liang, and L. Peng, "Plug-in gate-loop compensators for series-connected IGBT drivers in a solid-state fault current limiter," *CSEE J. Power Energy Syst.*, vol. 8, no. 1, pp. 165–174, Jan. 2022.

[14] Y. Zhong, Y. Xie, Y. Liu, H. Ye, J. Yuan, H. Zhou, and L. Wei, "A novel multi-function saturated-core fault current limiter," *IEEE Trans. Magn.*, vol. 55, no. 6, pp. 1–5, Jun. 2019.

[15] L. Jiang, J. X. Jin, and X. Y. Chen, "Fully controlled hybrid bridge type superconducting fault current limiter," *IEEE Trans. Appl. Supercond.*, vol. 24, no. 5, pp. 1–5, Oct. 2014.

[16] T. Hoshino, I. Muta, T. Nakamura, K. M. Salim, and M. Yamada, "Non-inductive variable reactor design and computer simulation of rectifier type superconducting fault current limiter," *IEEE Trans. Appl. Supercond.*, vol. 15, no. 2, pp. 2063–2066, Jun. 2005.

[17] A. D. Aliabad and S. H. Zarchi, "Optimal design and analysis of a variable reactor fault current limiter," *IET Electr. Power Appl.*, vol. 11, no. 9, pp. 1–8, Nov. 2017.

[18] M. Amini, A. D. Aliabad, and E. Amiri, "Design and analysis of fault current limiter based on air core variable series reactor," *IEEE Access*, vol. 9, pp. 166129–166136, 2021.

[19] M. Eladawy and I. A. Metwally, "A novel five-leg design for performance improvement of three-phase presaturated core fault-current limiter," *IEEE Trans. Magn.*, vol. 54, no. 7, pp. 1–10, Jul. 2018.

[20] B. Wang, C. Niu, H. He, Y. Wu, M. Rong, L. Wang, and J. Li, "Development of a hybrid fault current limiter using liquid metal for large capacity MVdc power systems," *IEEE Trans. Ind. Electron.*, vol. 69, no. 5, pp. 5050–5059, May 2022.

[21] J. Yuan, H. Zhou, Y. Zhong, P. Gan, Y. Gao, K. Muramatsu, Z. Du, and B. Chen, "Performance investigation on DCSFCL considering different magnetic materials," *AIP Adv.*, vol. 8, no. 5, May 2018, Art. no. 056621.

[22] R. Strumpler, J. Skindhoj, J. Glatz-Reichenbach, J. H. W. Kuhlefelt, and F. Perdoncin, "Novel medium voltage fault current limiter based on polymer PTC resistors," *IEEE Trans. Power Del.*, vol. 14, no. 2, pp. 425–430, Apr. 1999.

[23] S. A. Fazljoo, A. D. Aliabad, and E. Amiri, "A novel air core electromagnetic fault current limiter with rotational motion," *IET Electric Power Appl.*, early access, Mar. 2023, doi: 10.1049/elp2.12309.

[24] S. I. Babic and C. Akyel, "Calculating mutual inductance between circular coils with inclined axes in air," *IEEE Trans. Magn.*, vol. 44, no. 7, pp. 1743–1750, Jul. 2008.

[25] J. T. Conway, "Inductance calculations for noncoaxial coils using Bessel functions," *IEEE Trans. Magn.*, vol. 43, no. 3, pp. 1023–1034, Mar. 2007.
[26] J. C. Maxwell, *A Treatise on Electricity and Magnetism*. New York, NY, USA: Dover, 1954.
[27] K. B. Kim, E. Levi, Z. Zabar, and L. Birenbaum, "Mutual inductance of noncoaxial circular coils with constant current density," *IEEE Trans. Magn.*, vol. 33, no. 5, pp. 3916–3921, Sep. 1997.
[28] S. Babic, F. Sirois, C. Akyel, and C. Girardi, "Mutual inductance calculation between circular filaments arbitrarily positioned in space: Alternative to Grover's formula," *IEEE Trans. Magn.*, vol. 46, no. 9, pp. 3591–3600, Sep. 2010.
[29] P. L. Kalantarov and L. A. Zeitlin, *Calculation of Inductances*, 3rd ed. Saint Petersburg, Russia: Energoatomizdat (in Russia), 1986.
[30] S. Babic, F. Sirois, C. Akyel, G. Lemarquand, V. Lemarquand, and R. Ravaud, "New formulas for mutual inductance and axial magnetic force between a thin wall solenoid and a thick circular coil of rectangular cross-section," *IEEE Trans. Magn.*, vol. 47, no. 8, pp. 2034–2044, Aug. 2011.
[31] K.-B. Kim, E. Levi, Z. Zabar, and L. Birenbaum, "Restoring force between two noncoaxial circular coils," *IEEE Trans. Magn.*, vol. 32, no. 2, pp. 478–484, Mar. 1996.
[32] S. Babic and C. Akyel, "Magnetic force between inclined circular filaments placed in any desired position," *IEEE Trans. Magn.*, vol. 48, no. 1, pp. 69–80, Jan. 2012.
[33] Z. J. Wang and Y. Ren, "Magnetic force and torque calculation between circular coils with nonparallel axes," *IEEE Trans. Appl. Supercond.*, vol. 24, no. 4, pp. 1–5, Aug. 2014.
[34] X. Gou and J. Qin, "Analytic calculation of magnetic force between two current-carrying coils," *Appl. Math. Mech.*, vol. 36, no. 4, pp. 475–486, Apr. 2015.
[35] S. I. Babic and C. Akyel, "New formulas for calculating torque between filamentary circular coil and thin wall solenoid with inclined axis whose axes are at the same plane," *Prog. Electromagn. Res. M*, vol. 73, pp. 141–151, 2018.
[36] K. V. Poletkin and J. G. Korvink, "Efficient calculation of the mutual inductance of arbitrarily oriented circular filaments via a generalisation of the Kalantarov–Zeitlin method," *J. Magn. Magn. Mater.*, vol. 483, pp. 10–20, Aug. 2019.
[37] K. V. Poletkin, "Calculation of force and torque between two arbitrarily oriented circular filaments using Kalantarov–Zeitlin's method," 2021, *arXiv:2106.09496*.
[38] F. W. Grover, *Inductance Calculations: Working Formulas and Tables*. New York, NY, USA: Dover, 1964.
[39] P. C. Sen, *Electrical Machines*, 2nd ed. Hoboken, NJ, USA: Wiley, 1996, pp. 101–111.

SEYED AMIN FAZLJOO received the B.S. and M.S. degrees in electrical engineering. He is currently pursuing the Ph.D. degree with Yazd University. His research work is focused on fault current limiters. His research interests include electric machines, fault current limiters, and power electronics.

ALIAKBAR DAMAKI ALIABAD received the B.S., M.S., and Ph.D. degrees in electrical engineering from the Amirkabir University of Technology, Tehran, Iran, in 2005, 2007, and 2012, respectively. He is currently an Assistant Professor with the Electrical and Computer Engineering Faculty, Yazd University, Yazd, Iran. His main research interests include the design, analysis and manufacturing of electrical machines, fault current limiters, and power system dynamics.

EBRAHIM AMIRI (Senior Member, IEEE) received the B.Sc. and M.Sc. degrees in electrical engineering from the Amirkabir University of Technology, Tehran, Iran, in 2005 and 2008, respectively, and the Ph.D. degree in electrical engineering from Louisiana State University, Baton Rouge, LA, USA, in 2013. He is currently an Associate Professor and the Chair with the Department of Electrical Engineering, The University of New Orleans, New Orleans, LA, USA. His current research interests include the design, modeling, and optimization of electromagnetic devices.